

Mapping magnetic signals of individual magnetite grains to their internal magnetic configurations using micromagnetic models

David Cortés-Ortuño¹, Karl Fabian², and Lennart Vincent de Groot¹

¹Utrecht University

²Norwegian University of Science and Technology (NTNU)

November 23, 2022

Abstract

Micromagnetic Tomography (MMT) is a technique that combines X-ray micro computed tomography and scanning magnetometry data to obtain information about the magnetic potential of individual grains embedded in a sample. Recovering magnetic signals of individual grains in natural and synthetic samples provides a new pathway to study the remanent magnetization that carries information about the ancient geomagnetic field and is the basis of all paleomagnetic studies. MMT infers the magnetic potential of individual grains by numerical inversion of surface magnetic measurements using spherical harmonic expansions. The magnetic potential of individual particles in principle is uniquely determined by MMT, not only by the dipole approximation, but also more complex, higher order, multipole moments. Here we show that such complex magnetic information together with particle shape and mineralogy severely constrains the internal magnetization structure of an individual grain. To this end we apply a three dimensional micromagnetic model to predict the multipole signal from magnetization states of different local energy minima. We show that for certain grains it is even possible to uniquely infer the magnetic configuration from the inverted magnetic multipole moments. This result is crucial to discriminate single-domain particles from grains in more complex configurations such as multi-domain or vortex states. As a consequence, our investigation proves that by MMT it is feasible to select statistical ensembles of magnetic grains based on their magnetization states, which opens new possibilities to identify and characterize stable paleomagnetic recorders in natural samples.

1 Supporting Information for "Mapping magnetic
2 signals of individual magnetite grains to their
3 internal magnetic configurations using
4 micromagnetic models"

5 David Cortés-Ortuño¹, Karl Fabian², and Lennart V. De Groot¹

6 ¹Paleomagnetic laboratory Fort Hoofddijk, Department of Earth Sciences, Utrecht
7 University, Budapestlaan 17,, 3584 CD Utrecht, The Netherlands.

8 ²Norwegian University of Science and Technology (NTNU), S. P. Andersens veg 15a, 7031
9 Trondheim, Norway

10 February 16, 2022

11 S1 Magnetic signal of a single cuboid

12 In the manuscript the magnetic signal from a grain simulated with the micromagnetic
13 code was calculated by computing the dipole field of every magnetization vector in
14 the grain model. This allowed to compute the total magnetic flux produced by
15 the grain at a surface above it. To analyze the accuracy of this approximation a
16 test model is defined using a cuboidal particle. The stray field of this grain can
17 be calculated analytically and therefore the magnetic field it produces at a surface,
18 which can be compared directly with the simulated grain.

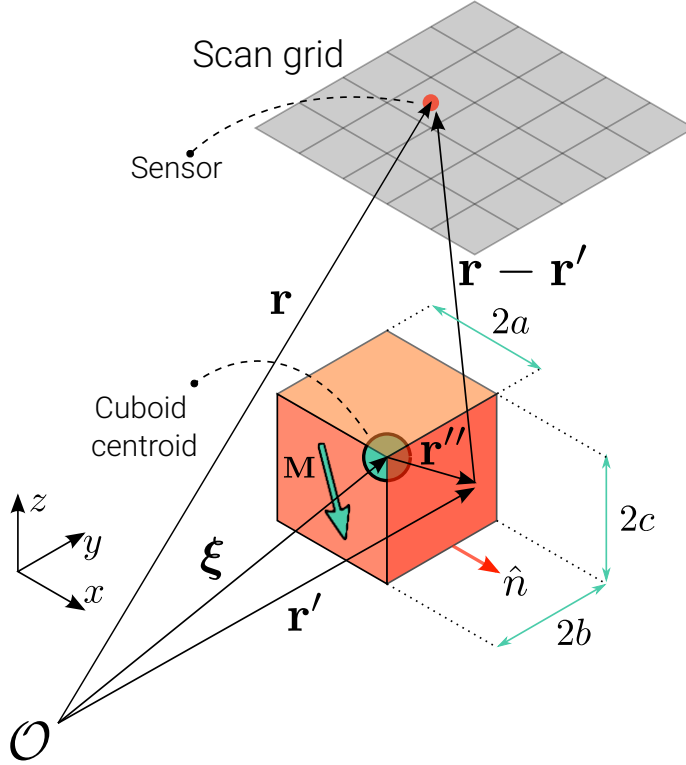
19 S1.1 Physical model

20 For a uniformly magnetized cuboid grain (located at the origin), the demagnetizing
21 field can be computed from the potential function that is defined over the boundary
22 surfaces (faces) $\partial\Omega$ of the cuboid as

$$\phi(\mathbf{r}) = \frac{1}{4\pi} \int_{\partial\Omega} \frac{\mathbf{M} \cdot d\mathbf{S}'}{|\mathbf{r} - \mathbf{r}'|}. \quad (1)$$

23 In equation 1, $d\mathbf{S}' = \hat{n} \cdot dS'$ is the surface element, with \hat{n} as the unit vector normal
24 to the faces, \mathbf{M} is the cuboid magnetization, \mathbf{r} is the location of the reference point
25 and the vectors \mathbf{r}' point to the locations of the magnetic sources, *i.e.* the cuboid faces
26 infinitesimal elements. This model is illustrated in Fig. S1, where position vectors
27 are defined with respect to an arbitrary origin \mathcal{O} . The magnetic field is defined as

$$\mathbf{B}(\mathbf{r}) = -\mu_0 \nabla \phi(\mathbf{r}). \quad (2)$$



SUPP. FIG. S1: Model system for the calculation of the stray field of a uniformly magnetized cuboid. Position vectors are defined with respect to an arbitrary origin \mathcal{O} . The scan grid is defined by a rectangular grid of sensor points in the xy -plane. The cuboid center is specified by the vector $\boldsymbol{\xi}$ such that the positions of infinitesimal cuboid face elements \mathbf{r}' are defined as $\mathbf{r}' = \boldsymbol{\xi} + \mathbf{r}''$, with \mathbf{r}'' as the location of the magnetic sources with respect to the cuboid center reference system.

28 For the case studied in the manuscript a single scan sensor is approximated as a
 29 physical point. Therefore, by defining $\gamma_B = \mu_0/(4\pi)$, the field component normal to
 30 a sensor grid point defined in the xy -plane is calculated as

$$B_z(\mathbf{r}) = -\mu_0 \frac{\partial}{\partial z} \left(\frac{1}{4\pi} \int_{\partial\Omega} \frac{\mathbf{M} \cdot d\mathbf{S}'}{|\mathbf{r} - \mathbf{r}'|} \right) \quad (3)$$

$$= -\gamma_B \int_{\partial\Omega} \mathbf{M} \cdot d\mathbf{S}' \frac{\partial}{\partial z} \left(\frac{1}{|\mathbf{r} - \mathbf{r}'|} \right) \quad (4)$$

$$= \gamma_B \int_{\partial\Omega} \mathbf{M} \cdot d\mathbf{S}' \frac{\partial}{\partial z'} \left(\frac{1}{|\mathbf{r} - \mathbf{r}'|} \right) \quad (5)$$

31 In equation 5 the derivative variable was changed, which is more convenient for two
 32 of the cuboid faces. The integral limits can be simplified if the integration variable is
 33 changed to the coordinate system of the cuboid center $\boldsymbol{\xi}$ by noticing that $\mathbf{r}' = \boldsymbol{\xi} + \mathbf{r}''$,
 34 as shown in Fig. S1. In this case $d\mathbf{S}' = d\mathbf{S}''$ and $\frac{\partial f}{\partial z'} = \frac{\partial f}{\partial z''}$ for an arbitrary function
 35 f , hence the field can be expressed as

$$B_z(\mathbf{r}) = \gamma_B \int_{\partial\Omega} \mathbf{M} \cdot d\mathbf{S}'' \frac{\partial}{\partial z''} \left(\frac{1}{|\mathbf{r} - (\boldsymbol{\xi} + \mathbf{r}'')|} \right) \quad (6)$$

$$= \gamma_B \int_{\partial\Omega} \mathbf{M} \cdot d\mathbf{S}'' \frac{\partial}{\partial z''} \left(\frac{1}{|\mathbf{X} - \mathbf{r}''|} \right) \quad (7)$$

36 with $\mathbf{X} = \mathbf{r} - \boldsymbol{\xi}$. Alternatively, the field can also be written as

$$B_z(\mathbf{r}) = -\gamma_B \frac{\partial}{\partial z} \int_{\partial\Omega} \mathbf{M} \cdot d\mathbf{S}'' \left(\frac{1}{|\mathbf{X} - \mathbf{r}''|} \right) \quad (8)$$

37 To compute the integrals we refer to (Hubert & Schäfer 1998, p. 122) where
 38 integrations are carried out based on the source function $F_{000}(r)$ such that

$$r = \sqrt{x^2 + y^2 + z^2} \quad (9)$$

$$L_x = \operatorname{arctanh}\left(\frac{x}{r}\right) \quad (10)$$

$$P_x = x \operatorname{arctan}\left(\frac{yz}{xr}\right) \quad (11)$$

$$F_{000} = \left(\frac{1}{r}\right) \quad (12)$$

$$F_{100} = \int F_{000} dx = L_x \quad (13)$$

$$F_{110} = \int F_{100} dy = yL_x + xL_y - P_z \quad (14)$$

$$F_{11-1} = \frac{\partial}{\partial z} F_{110} = -\operatorname{arctan}\left(\frac{xy}{zr}\right) \quad (15)$$

39 Using equation 7 it is now possible to compute the field contribution of the cuboid
 40 face in the yz -plane, where $x'' = a$ and $\hat{n} = +\hat{x}$, as

$$B_z^{[+\hat{x}]}(\mathbf{r}) = \gamma_B M_x \int_{y''=-b}^{y''=+b} \int_{z''=-c}^{z''=+c} dy'' dz'' \frac{\partial}{\partial z''} \left(\frac{1}{|\mathbf{X} - \mathbf{r}''|} \right) \Bigg|_{x''=+a} \quad (16)$$

$$= \gamma_B M_x \int_{y''=-b}^{y''=+b} dy'' \left(\frac{1}{|\mathbf{X} - \mathbf{r}''|} \right) \Bigg|_{x''=+a} \Bigg|_{z''=-c}^{z''=+c} \quad (17)$$

$$= \gamma_B M_x \int_{y''=-b}^{y''=+b} dy'' F_{000}(\mathbf{X} - \mathbf{r}'') \Bigg|_{x''=+a} \Bigg|_{z''=-c}^{z''=+c} \quad (18)$$

$$= -\gamma_B M_x F_{010}(|\mathbf{X} - \mathbf{r}''|) \Bigg|_{x''=+a} \Bigg|_{z''=-c}^{z''=+c} \Bigg|_{y''=-b}^{y''=+b} \quad (19)$$

$$= -\gamma_B M_x F_{010}(\mathbf{r} - [\boldsymbol{\xi} + \mathbf{r}'']) \Bigg|_{x''=+a} \Bigg|_{z''=-c}^{z''=+c} \Bigg|_{y''=-b}^{y''=+b} \quad (20)$$

$$= -\gamma_B M_x F_{010}(x - \xi - a, y - \eta - y'', z - \zeta - z'') \Bigg|_{x''=+a} \Bigg|_{z''=-c}^{z''=+c} \Bigg|_{y''=-b}^{y''=+b} \quad (21)$$

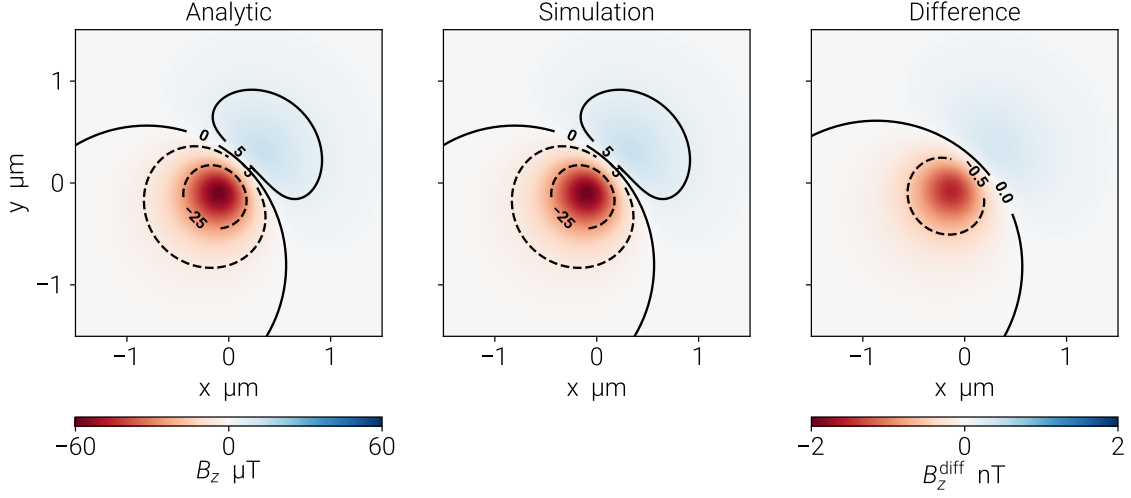
41 Similarly, for the opposite face with normal in the $-\hat{x}$ direction the resulting field
42 is

$$B_z^{[-\hat{x}]}(\mathbf{r}) = -\gamma_B (-M_x) F_{010}(\mathbf{r} - [\boldsymbol{\xi} + \mathbf{r}'']) \Bigg|_{x''=-a} \Bigg|_{z''=-c}^{z''=+c} \Bigg|_{y''=-b}^{y''=+b}, \quad (22)$$

43 and for the faces in the xz -planes (normals in the $\pm\hat{y}$ directions) the field expressions
44 are

$$B_z^{[\pm\hat{y}]}(\mathbf{r}) = -\gamma_B (\pm M_y) F_{100}(\mathbf{r} - [\boldsymbol{\xi} + \mathbf{r}'']) \Bigg|_{y''=\pm b} \Bigg|_{z''=-c}^{z''=+c} \Bigg|_{x''=-a}^{x''=+a}. \quad (23)$$

45 Finally, for the faces in the xy -planes (normals in the $\pm\hat{z}$ directions), the field is



SUPP. FIG. S2: Comparison of the stray field of the uniformly magnetized cuboid model computed from both an analytical formulation and a micromagnetic simulation. The cuboid is defined as a cube of 50 nm edge size with its center at $z = -35$ nm. The stray field is calculated at a height of $z = 500$ nm.

46 computed using equation 8 to obtain

$$B_z^{[\pm z]}(\mathbf{r}) = -\gamma_B (\pm M_z) \frac{\partial}{\partial z} \left[\int_{x''=-a}^{x''=+a} \int_{y''=-b}^{y''=+b} dx'' dy'' \left(\frac{1}{|\mathbf{X} - \mathbf{r}''|} \right) \right] \Bigg|_{z''=\pm c} \quad (24)$$

$$= -\gamma_B (\pm M_z) \frac{\partial}{\partial z} [(-1)^2 F_{110}(\mathbf{r} - [\boldsymbol{\xi} + \mathbf{r}''])] \Bigg|_{z''=\pm c} \Bigg|_{y''=-b}^{y''=+b} \Bigg|_{x''=-a}^{x''=+a} \quad (25)$$

$$= -\gamma_B (\pm M_z) F_{11-1}(\mathbf{r} - [\boldsymbol{\xi} + \mathbf{r}'']) \Bigg|_{z''=\pm c} \Bigg|_{y''=-b}^{y''=+b} \Bigg|_{x''=-a}^{x''=+a} \quad (26)$$

Order: Dipole	
Magnetization	: 479998.6572 A/m
Dipole moments (norm):	(0.5774 0.5774 -0.5774)
Bres _F / B _F	: 7.3496e-06
Largest residual	: -0.0009 μ T
Largest Bz	: -58.3056 μ T

Order: Quadrupole	
Magnetization	: 480003.7494 A/m
Dipole moments (norm):	(0.5774 0.5774 -0.5774)
Bres _F / B _F	: 5.2152e-06
Largest residual	: -0.0006 μ T
Largest Bz	: -58.3056 μ T

Order: Octupole	
Magnetization	: 480170.2555 A/m
Dipole moments (norm):	(0.5778 0.5771 -0.5771)
Bres _F / B _F	: 2.4465e-04
Largest residual	: 0.0053 μ T
Largest Bz	: -58.3056 μ T

SUPP. TABLE S1: Results of multipole inversions of different order applied to the test cuboid system.

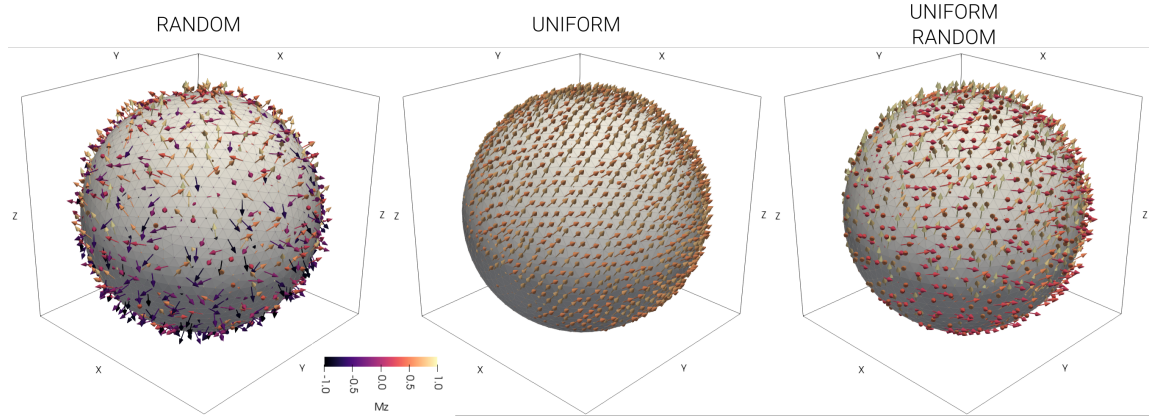
47 **S1.2 Cuboid test model**

48 The theoretical results obtained for the stray field of a cuboid particle are compared
49 to the results obtained from a micromagnetic simulation using the finite element code
50 MERRILL (Ó Conbhuí *et al.* 2018). A cuboid of dimensions $50 \text{ nm} \times 50 \text{ nm} \times 50 \text{ nm}$
51 is defined with its center at $z = -35 \text{ nm}$. In addition, the particle's magnetization is
52 specified with a magnitude of $|\mathbf{M}| = 0.48 \text{ MA/m}$ and orientation $\mathbf{M}/|\mathbf{M}| = 0.577 \times$
53 $(1, 1, -1)$. The z -component of the stray field for both the theoretical and simulation
54 models are calculated on a scan grid of size $1.5 \mu\text{m} \times 1.5 \mu\text{m}$ at a height position of
55 $z = 0.5 \mu\text{m}$. A comparison of the stray field results is shown in Fig. S2. The
56 relative error of the simulation with respect to the theoretical solution in this case is

57 estimated as $B_{\text{err}} = \|B_z^{\text{sim}} - B_z^{\text{theory}}\|_F / \|B_z^{\text{theory}}\|_F = 2.7183 \times 10^{-5}$. This small value
58 confirms that the stray field approximation of the micromagnetic simulation, where
59 the magnetization vectors at finite element nodes are treated as point dipoles, is in
60 excellent agreement with the analytical formulation. Therefore the micromagnetic
61 simulation can be used as a model to analyze the stray field signal of more complex
62 magnetic structures.

63 Numerical inversions of the micromagnetic model of the test cuboid system were
64 performed using multipole expansions up to the octupole order. The results of these
65 inversions are summarized in Table S1 where the small relative error of the residuals
66 indicate that the inverted stray field is approximated with high accuracy, which is
67 supported by the correct magnitudes of the inverted magnetization and the inverted
68 dipole moments. In particular, a dipole order expansion is sufficient to reproduce
69 the right values of the cuboid magnetization.

70 **S2 Initial states for the magnetite sphere**

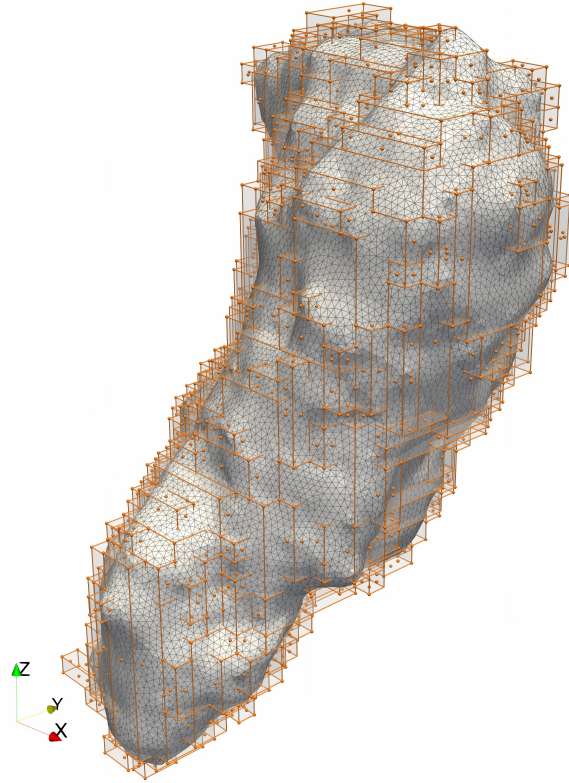


SUPP. FIG. S3: Visualization of the initial states used for the simulations of a magnetite sphere using the MERRILL code. The selected uniform states are used to obtain magnetic states oriented in the $[101]$ direction. Arrows depict the normalized magnetization vectors which are colored by their z -component. The titles indicate the type of initial state used in the simulations. For the RANDOM configuration, the `Randomize All Moments` command was used. For the UNIFORM configuration, the `Uniform Magnetization 1.00 0.00 1.00` command together with `Randomize Magnetization 10` were used. For the UNIFORM RANDOM state the random component was specified with a value of 35 degrees. In the manuscript, the uniform states are specified in 26 different directions in the Cartesian plane.

71 **S3 Surface reconstruction**

72 The generation of the finite element mesh for the grain 4 of Area 2 defined in the
73 synthetic sample of (de Groot *et al.* 2018b) requires to reconstruct a surface that
74 can be partitioned into tetrahedral units. This surface can be generated from an
75 unstructured cloud of points which, in this case, is obtained from the the microCT
76 data. Specifically, in (de Groot *et al.* 2018b) the voxel representation of the grains
77 from the microCT data is transformed into a cuboid decomposition of the grains
78 where voxels are grouped into cuboids of maximal available size that fit within the
79 grain geometry with an efficient final representation of the grain shape. For the
80 reconstruction of the grain surface, a cloud of points is specified by taking both the
81 cuboid vertices and the center of every cuboid face, in order to produce more points
82 for the reconstruction algorithm. This point data is publicly available in (de Groot
83 *et al.* 2018a) for the synthetic sample of (de Groot *et al.* 2018b). In the case of
84 grain 4, the cuboid decomposition together with the cuboid vertices and cuboid face
85 centers are shown in Fig. S4. For this model the grain size was downscaled to 2% of
86 the original grain size.

87 Optimized algorithms using unstructured set of points are implemented in the
88 Computational Geometry Algorithms Library (CGAL) (The CGAL Project 2021).
89 For the model used in the manuscript, the Poisson Surface Reconstruction (PSR) (Al-
90 liez *et al.* 2021) was applied, which requires a calculation of the normal vectors
91 at every point. The calculation of the normals was achieved using the `CGAL::`
92 `jet_estimate_normals` function and consequently the normals were oriented with
93 the `CGAL::mst_orient_normals` function. To generate a surface with the PSR algo-



SUPP. FIG. S4: Surface reconstruction and finite element mesh for the magnetic grain 4 in the synthetic sample of (de Groot *et al.* 2018b). The decomposition of the grain into cuboids (by grouping voxels from microCT data) is shown by transparent structures with orange edges and was obtained from the grain data in (de Groot *et al.* 2018a). Cuboid vertices and face centers are depicted as small spheres. The surface was constructed via the Poisson Surface Reconstruction algorithm and the volume was partitioned into tetrahedral units.

94 rithm the function `CGAL::poisson_surface_reconstruction_delaunay` was used.
 95 The resulting surface is depicted in Fig. S4, which shows that the algorithm approxi-
 96 mates grain geometry efficiently. An improved surface reconstruction can be achieved
 97 in the future by using the voxel representation of the grains from the microCT data

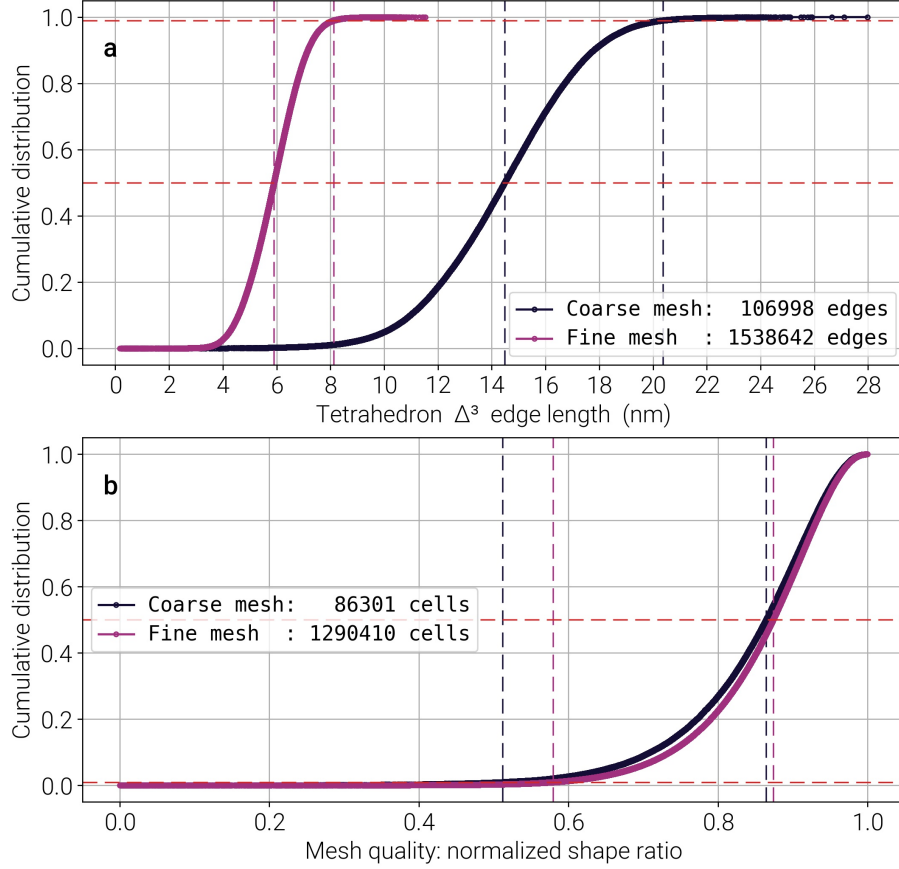
98 directly.

99 The final step to obtain a finite element mesh for the micromagnetic simula-
100 tions is to partition the volume defined by the reconstructed surface into tetra-
101 hedrons with edge lengths smaller than the exchange length of the material. As
102 specified in the main manuscript, the CGAL library contains *tetrahedralization* al-
103 gorithms. In particular, for the grain 4 model the Tetrahedral Isotropic Remeshing
104 method (Tournois *et al.* 2021) was applied, which is based on the Multi-Material
105 Adaptive Volume Remesher algorithm. The tetrahedralization of the grain 4 sur-
106 face was achieved by firstly, generating a three dimensional volume mesh using
107 the `CGAL::make_mesh_3` function and consequently refining this mesh with the re-
108 meshing function `CGAL::tetrahedral_isotropic_remeshing`. This last method
109 produced more efficient results (more consistent edge length sizes) than refining the
110 mesh with the `CGAL::refine_mesh_3` function, and was implemented in one of the
111 latest CGAL releases with version number 5.1.

112 The CGAL code generates the mesh in `.mesh` format while the MERRILL code
113 accepts both PATRAN `.neu` and Tecplot `.tec` mesh formats. Therefore, to con-
114 vert the mesh for the grain model the meshio (Schlömer 2021) code is used with
115 modifications from the authors of this work.

116 **S3.1 Energy minimization and mesh statistics**

117 Finding metastable magnetic configurations in a mesh with substantial number of
118 nodes is a computationally cost calculation. In particular when the system is initial-
119 ized with randomly oriented magnetization vectors because the algorithm requires



SUPP. FIG. S5: Statistical data of the finite element mesh for the magnetite grain model from a synthetic sample at room temperature. (a) Cumulative distribution of the edge lengths of the mesh tetrahedra for both a coarsely and finely discretized mesh. Vertical lines indicate the 50th and 99th percentiles. (b) Mesh quality of tetrahedra, or cells, using the normalized shape ratio parameter (Field 1991) (see discussion in text). Vertical lines indicate the 1st and 50th percentiles.

120 to find LEM states in a complex energy landscape by following different paths that
 121 minimize the micromagnetic energy. To speed up the process of energy minimization
 122 for the grain model of the synthetic sample, the strategy used in the paper is:

- 123 • Define a coarsely discretized mesh, *i.e.* using tetrahedra with edge lengths

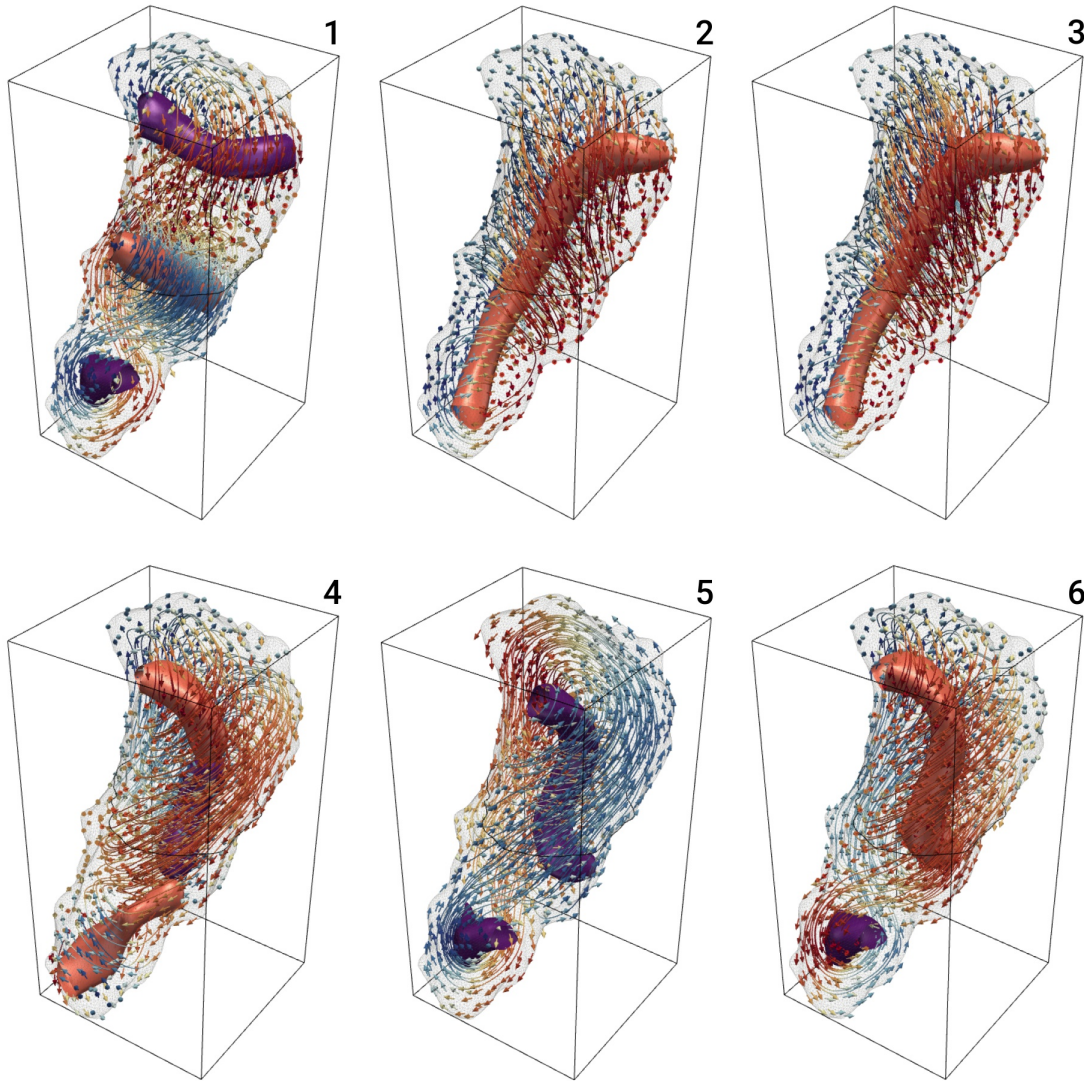
124 larger than the material's exchange length ℓ_{ex} .

- 125 • Start the minimization and find a candidate for a LEM.
- 126 • Define the *physically correct* mesh using tetrahedron's edge lengths smaller
127 than ℓ_{ex} .
- 128 • Interpolate the magnetization field of the LEM found with the coarse mesh
129 into the magnetization field of the refined mesh. This feature is implemented
130 in the MERRILL code.
- 131 • Minimize the energy of the refined mesh using a Conjugate Gradient method
132 in Cartesian coordinates and find a LEM.

133 Statistics of the FEM tetrahedra, or cells, for the mesh of the grain model of the
134 synthetic sample (see Fig. S4) are detailed in Fig.S5. Plot (a) shows the cumulative
135 distribution of edge lengths for both the coarse and fine meshes. In the case of the
136 fine mesh, the 50th and 99th percentiles of the edge lengths are located at 5.90 nm
137 and 8.12 nm, respectively, which are smaller than $\ell_{\text{exch}} = 9.59$ nm of magnetite at
138 room temperature. For the coarse mesh the 99th percentile is located at 20.37 nm.
139 Furthermore, the number of tetrahedron edges for the fine mesh is an order of mag-
140 nitude larger than that of the modeled coarse mesh and its distribution is narrower
141 than that of the coarse mesh. Plot (b) depicts a quantification of the quality of the
142 meshes by means of a normalized shape ratio (Field 1991). For every tetrahedron
143 cell, which is a 3-simplex, this parameter is defined as the ratio of the radius of the
144 sphere inscribed in the cell (inradius) divided by the radius of the sphere enclosing

145 the cell (circumradius), multiplied by the circumradius to inradius ratio of the reg-
146 ular k -simplex, or simply the cell dimension, which in this case is 3. Meshes with
147 normalized shape ratios closer to 1 translates into a good mesh quality, since the cells
148 are close to regular tetrahedra. Tetrahedrons with ratios closer to zero are poorly
149 defined by having edges with large variations in size or are flat in shape, which can
150 affect the convergence of the algorithm (Ó Conbhuí *et al.* 2018). For the fine mesh
151 the 1st and 50th percentile are 0.58 and 0.87, respectively. For the coarse mesh the
152 1st percentile is located at 0.51. These mesh statistics were computed using the
153 Dofin (Logg & Wells 2010) finite element code.

154 **S4 Synthetic sample states**



SUPP. FIG. S6: Magnetic configurations obtained after energy minimization of the grain 4 of Area 2 of the synthetic sample of (de Groot *et al.* 2018b), starting from six different states where magnetization vectors are randomly oriented. In the main manuscript, configurations 1, 5 and 6 were chosen to perform numerical inversions of the stray field produced by them.

155 References

- 156 1. Alliez, P., Saboret, L. & Guennebaud, G. in *CGAL User and Reference Manual*
157 5.3 (CGAL Editorial Board, 2021). [https://doc.cgal.org/5.3/Manual/
158 packages.html#PkgPoissonSurfaceReconstruction3](https://doc.cgal.org/5.3/Manual/packages.html#PkgPoissonSurfaceReconstruction3).
- 159 2. de Groot, L. V. *et al.* *List of grains and results of the Scanning SQUID Mag-*
160 *netometer (SSM) scan data set.* 2018. [https://doi.org/10.1594/PANGAEA.
161 886724](https://doi.org/10.1594/PANGAEA.886724).
- 162 3. De Groot, L. V. *et al.* Determining Individual Particle Magnetizations in As-
163 semblages of Micrograins. *Geophysical Research Letters* **45**, 2995–3000. [https:
164 //agupubs.onlinelibrary.wiley.com/doi/abs/10.1002/%202017GL076634
165 \(2018\)](https://agupubs.onlinelibrary.wiley.com/doi/abs/10.1002/%202017GL076634).
- 166 4. Field, D. A generic Delaunay triangulation algorithm for finite element meshes.
167 *Advances in Engineering Software and Workstations* **13**, 263–272. ISSN: 0961-
168 3552. [https://www.sciencedirect.com/science/article/pii/096135529190031X
169 \(1991\)](https://www.sciencedirect.com/science/article/pii/096135529190031X).
- 170 5. Hubert, A. & Schäfer, R. *Magnetic Domains: The Analysis of Magnetic Mi-*
171 *crostructures* ISBN: 9783540641087 (Springer, Berlin, Heidelberg, 1998).
- 172 6. Logg, A. & Wells, G. N. DOLFIN: Automated Finite Element Computing.
173 *ACM Trans. Math. Softw.* **37**. ISSN: 0098-3500. [https://doi.org/10.1145/
174 1731022.1731030](https://doi.org/10.1145/1731022.1731030) (Apr. 2010).
- 175 7. Ó Conbhuí, P. *et al.* MERRILL: Micromagnetic Earth Related Robust Inter-
176 preted Language Laboratory. *Geochemistry, Geophysics, Geosystems* **19**, 1080–

- 177 1106. eprint: <https://agupubs.onlinelibrary.wiley.com/doi/pdf/10.1002/2017GC007279>. <https://agupubs.onlinelibrary.wiley.com/doi/abs/10.1002/2017GC007279> (2018).
- 178
- 179
- 180 8. Schlömer, N. *meshio: Tools for mesh files* version v5.0.2. Github: <https://github.com/nschloe/meshio>. Sept. 2021. <https://doi.org/10.5281/zenodo.5541160>.
- 181
- 182
- 183 9. The CGAL Project. *CGAL User and Reference Manual* 5.3. <https://doc.cgal.org/5.3/Manual/packages.html> (CGAL Editorial Board, 2021).
- 184
- 185 10. Tournois, J., Faraj, N., Thiery, J.-M. & Boubekur, T. in *CGAL User and Reference Manual* 5.3 (CGAL Editorial Board, 2021). <https://doc.cgal.org/5.3/Manual/packages.html#PkgTetrahedralRemeshing>.
- 186
- 187